D3.1
Inspection sensitivity analysis

General information	
Grant agreement number	755500
Start date of the project	01/09/2017
Project duration	48 months
Due date of the deliverable	31/08/2018
Actual submission date	28/02/2019
Lead beneficiary	6 – UoB

Keywords
Ultrasonic arrays, defect characterisation, scattering matrix, grain scattering noise

Type	Meaning	
R	Document, report	x
DEM	Demonstrator, pilot, prototype	
DEC	Websites, patent fillings, videos, etc.	
OTHER	Software, technical diagram, etc.	

Dissemination Level		
PU	Public	x
CO	Confidential, only for members of the consortium (including the Commission Services)	

Table of Content

Table of Tables

Table of Figures

Glossary

Abbreviations/Acronym	Description
FE	Finite Element
FMC	Full Matrix Capture
GPU	Graphics Processing Unit
IWEX	Inverse Wave Field Extrapolation
NDT	Non-Destructive Testing
PCA	Principal Component Analysis
SNR	Signal-to-Noise Ratio
TFM	Total Focusing Method

1 Summary

This report aims to study the inspection performance of ultrasonic testing for detection and characterisation of defects in coarse grained materials. In particular, the use of the scattering matrix, extractable from the FMC dataset, is explored and it is shown that the proposed method using the scattering matrix can facilitate improved detection and characterisation of defects compared to methods based on ultrasonic images. The first step of the proposed method is accurate modelling of the grain scattering noise. Multiple realisations of the grain structure are simulated to understand the influence of the coarse-grained material on both defect detection and characterisation. As an example, assuming an average grain size of 0.2mm, cracks and holes of sizes between 1mm and 3mm are considered at frequencies 1-3 MHz. This modelling framework is shown to be suitable to understand the influence of the material and array imaging parameters on both the detection and characterisation problems in coarse-grained materials.

2 Introduction

Ultrasonic inspection is a widely used technique in non-destructive testing (NDT) [1], [2]. An important application can be found for inspection of nuclear power plants, where ultrasound is often considered to be preferable to radiography due to the safety concerns related to the use of X-rays [3]. In recent years, the capability of using ultrasound to detect and characterise defects has improved significantly with the introduction of transducer arrays [4] and advanced imaging algorithms, such as the total focusing method (TFM) [5], the inverse wave field extrapolation (IWEX) method [6], and the wavenumber algorithm [7]. Alternatively, when the defect is relatively small (*i.e.* less than two wavelengths in size), the far-field scattering matrix can be extracted from the array data and used for accurate characterisation [8].

Like other inspection techniques, the performance of ultrasonic inspection is subject to measurement noise and can potentially become very poor if the signal-to-noise ratio (SNR) of the measurement is low. One of the main challenges for inspecting nuclear power plant components is caused by the existence of grains in the material (*i.e.* polycrystalline materials that are widely used in nuclear industry [9]). Ultrasonic attenuation and backscatter caused by the interaction of the ultrasonic waves with the grains can severely affect the SNR of the measured signals and resultant images. High-frequency inspection and/or materials with large grains are particularly challenging because attenuation increases with the grain size and frequency for grain sizes of practical interest [10]. For example, in the Rayleigh regime (*i.e.* grain size is much smaller than the wavelength), the attenuation coefficient is proportional to the fourth power of the frequency and the third power of the grain size [10], suggesting that low-frequency inspection should be used in order to detect small defects [11]. Low frequencies are, however, undesirable for defect characterisation because of the poor imaging resolution. The grains also cause backscattered echoes to be contaminated with coherent noise [12]. The amplitude and shape of the defect signal can be affected by the coherent noise, making it difficult to distinguish the defect signal from signals measured from defect-free regions of a component.

A parametric-manifold mapping approach [8] is adopted in this report for detection and characterisation of defects using the scattering matrix. The defect manifold (representing scattering matrices of all possible defects of a given type) and noise model (describing how the measured scattering matrices differ from the modelled ones) are two key components of the characterisation procedure [8]. Compared with approaches based on typical machine learning algorithms (*e.g.* classification of the defect type using support vector machine classifiers [13]), this approach has the advantage that it can visualise and explain the characterisation process by exploring the geometry of the defect manifold. In addition, it was shown using Bayes theorem that the characterisation uncertainty can be quantified by adopting a proper noise model [8]. In the current work, we aim to use more accurate noise models for improved detection and characterisation when the noise is caused by grain scattering [14]. By using accurate noise models for evaluation of the characterisation uncertainty, significant improvement is achieved for detection/characterisation of defects in coarse grained materials compared with methods based on ultrasonic images as well as methods using general noise models.

3 Forward modelling

3.1 Grain scattering modelling

Accurate forward modelling provides the basis for any inversion technique. In this report, we adopted the finite element (FE) modelling approach proposed in [15] to simulate the ultrasonic signals scattered by a grain structure in 2D. A random grain structure can be obtained with the use of Voronoi diagrams [16], and below is a brief description of the approach. More details about the forward modelling procedure, including FE modelling of 3D structures, can be found in [15].

The first step in simulating a grain structure is to create uniform grid points within the sample. The grid points are then shifted by a random amount that follows a Gaussian distribution. The spacing of the initial grid points determines the average grain size, and the standard deviation of the Gaussian distribution (termed the shift parameter hereafter) is linked to the grain size variation of the final structure. A Voronoi diagram is created based on these randomly distributed grid points (nodes), and Fig. 1(a) shows an example of the Voronoi diagram in a 5mm×5mm region. As can be seen, the Voronoi diagram divides the sample region into a number of convex polygons, each containing one node and defining the region of the diagram that is closest to the node [11]. To model a quasi-isotropic material such as Type 304 stainless steel, each grain is assumed to have a random orientation [15]. We note that Type 304 stainless steel is commonly used in pressure vessels in the nuclear power industry and assume the grain parameters $c_{11} = 2.16 \times 10^{11}\ \mathrm{N/m^2}$, $c_{12} = 1.45 \times 10^{11}\ \mathrm{N/m^2}$, $c_{44} = 1.29 \times 10^{11}\ \mathrm{N/m^2}$, and $\rho = 7860\ \mathrm{kg/m^3}$ (c_{11}, c_{12}, and c_{44} are elastic constants of a cubic material) [17], [18].

Figure 1(b) shows the measurement configuration adopted in this report. A 64 element linear array with an element pitch of 0.5mm is used on a sample with the depth of 40mm. The excitation signal is chosen to be a wideband input signal with a centre frequency of 2.5 MHz. Hence, the received signal is also wide-band (although containing less high frequency contents due to attenuation), which enables us to extract defect (and noise) data and compare imaging/characterisation results at different frequencies. In this report, imaging and scattering matrix extraction are performed for frequencies between 1 MHz and 3 MHz, and the array is always Nyquist spatially-sampled (*i.e.* element pitch is smaller than half the wavelength) within this frequency range. The target defect is located at a distance of 20mm from the surface, and it is aligned with the array centre. A 5mm side-drilled hole is introduced on the right-hand-side of the defect as a reference scatterer. Multiple measurement data for a given defect are needed to calculate the statistics of the grain noise distribution. The array data are simulated from different realisations of the grain structure, with Pogo [19] being used as the FE solver. Pogo has the advantage of utilising the computational power of graphics processing units (GPUs) and is reported to reduce the processing time by up to 200 times compared to a CPU-based commercial software [19]. A regular mesh is used in FE for computational efficiency, and the grain boundaries are modified to match the meshes in FE. The element size used in this report is 80 μm, which corresponds to 23 elements per wavelength at the highest frequency considered for imaging and characterisation (*i.e.* 3 MHz). This gives typical run time of 36 minutes for an FE model having 8.7×10^5 degrees of freedom and 8.6×10^5 elements, based on an Nvidia Quadro 600 GPU. 50 random grain structures having the mean grain size of 0.2mm are simulated using the procedure described above where the shift parameter is set to be 0.4mm, giving grain structures similar to the one shown in Fig. 1(a). A simulated sample typically has 65,000 grains and Fig. 1(c) shows the grain size distribution which is seen to follow a Gaussian distribution. Defects can be introduced by removing certain elements at the defect location according to the desired defect geometry, and the shapes of the defects thus follow the edges of the regular mesh. Cracks and holes of sizes 1mm, 2mm, and 3mm are chosen as target defects, and the random grain structures are used to simulate array data of the target defects. In addition, defect-free data for each of the

grain structures are also simulated. It is worth pointing out that the main aim of this report is to study the grain scattering phenomenon and develop a defect charactersiation approach which can address issues related to grain scattering noise. The characterisation approach developed in this report can be applied to a wide range of grain (and defect) sizes, and discussions on the fundamental limits of the achievable characterisation performance are included in *Deliverable 3.2* of WP3.

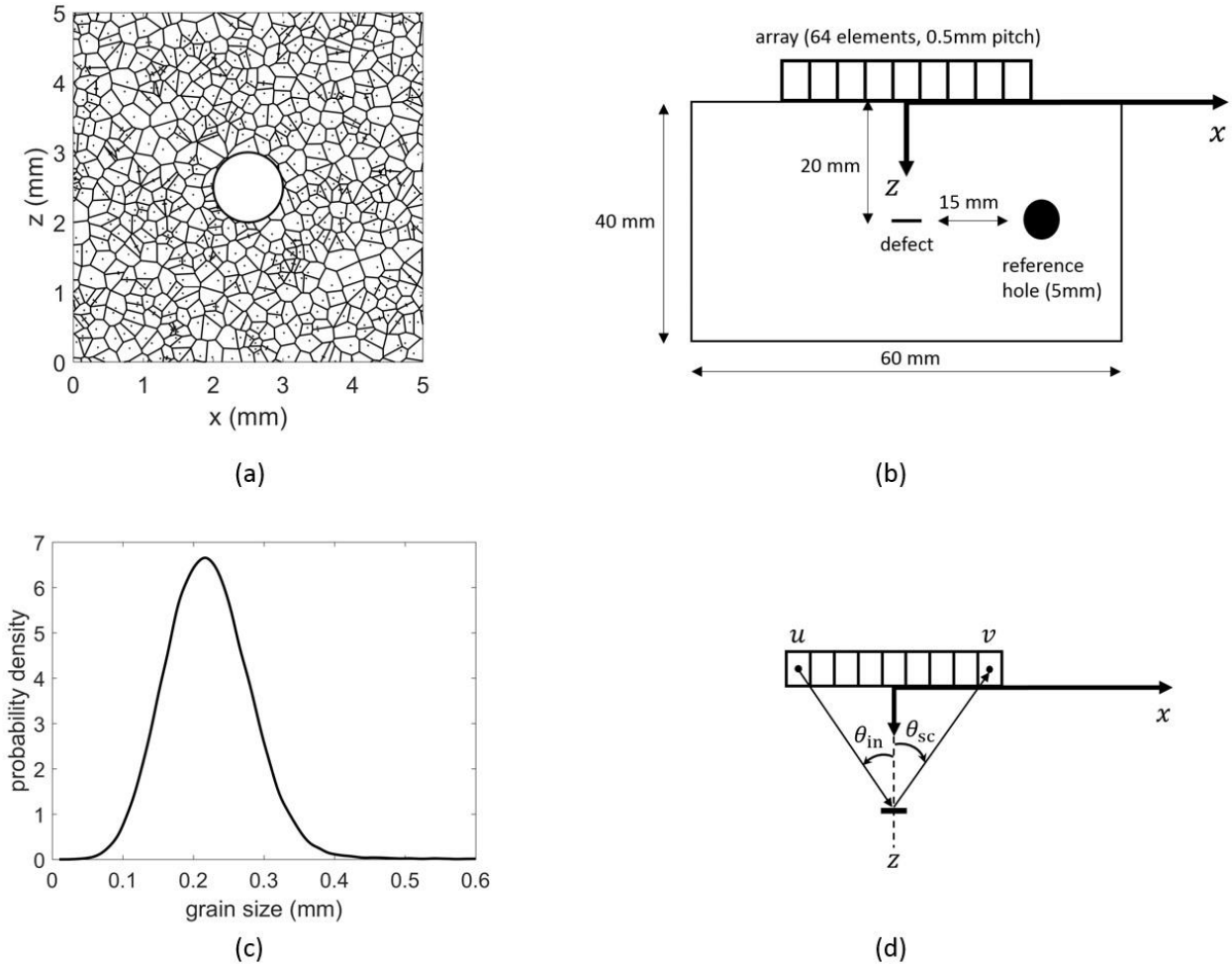

Figure 1: (a) An example grain structure with a 1mm side-drilled hole at the centre, (b) measurement configuration adopted in FE modelling, (c) grain size distribution of the simulated samples, and (d) notation used for imaging and defining the scattering matrix. In (a) and (c), the mean grain size and shift parameters are 0.2mm and 0.4mm. In (d), an incident angle $\boldsymbol{\theta_{in}}$ (or a scattering angle $\boldsymbol{\theta_{sc}}$) is positive if it is measured clockwise from the z -axis.

3.2 Calculation of the ultrasonic velocity and attenuation

High resolution imaging algorithms such as the total focusing method (TFM) [5] work by synthetically focusing the ultrasonic beam at each pixel point. Focusing is achieved by calculation of delay laws for different array elements based on the propagation distance and the ultrasonic velocity [20]. In addition, amplitude reduction caused by attenuation should be compensated for when extracting scattering matrices from the array data. In this section, the ultrasonic velocity and frequency-dependent attenuation coefficients are calculated from simulated time domain data using the first and second back wall reflections from a defect-free sample [11]. For this purpose, 20 defect-free samples of 10mm depths are simulated separately for the same mean grain size of 0.2mm. An equivalent pulse-echo signal is obtained by averaging signals recorded by all transmitter-receiver pairs of the 64 element array (element pitch: 0.5mm) for all 20 simulations (see Fig. 2(a)). Averaging

the time-domain signal of all tranmitter-receiver pairs of an array is equaivalent to using the array as a large unfocused monolithic transducer, and hence, the effecs of beam spreading become negligible [21]. The ultrasonic velocity can be calculated based on the difference in the arrival times of the first and second back wall reflections. The attenuation coefficient is calculated by [11]

$$\alpha(\omega) = \frac{1}{2d} ln \left| \frac{Q_1(\omega)}{Q_2(\omega)} \right|, \tag{1}$$

where $Q_1(\omega)$ and $Q_2(\omega)$ are frequency spectra of the first and second back wall reflections, respectively, and d=10mm is the depth of the sample. The attenuation coefficient results are shown in Fig. 2(b). A cubic line (dashed line in Fig. 2(b)) is fitted to data within the usable bandwidth (*i.e.* between 1.1 MHz and 2.4 MHz) to obtain attenuation coefficients within the whole frequency range considered. This follows from the relationship $\alpha \propto d^2 k^3$ between the attenuation coefficient α, grain size d, and wavenumber $k = \omega/c$ in the Rayleigh regime assuming a 2D geometry [10].

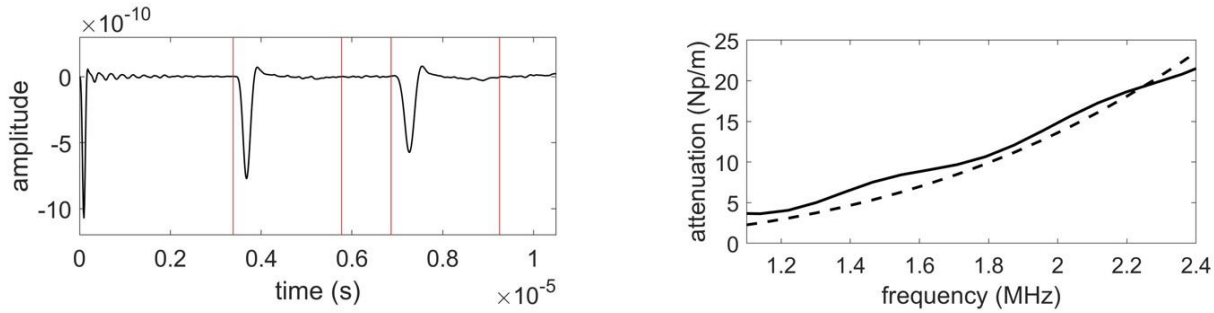

(a) (b)

Figure 2: (a) Equivalent pulse-echo signal, and (b) attenuation coefficients (dashed line shows the result of the cubic fit). Also shown in (a) are the FFT windows used for calculating the frequency spectra of the first and second back wall reflections.

4 Imaging results and SNR calculations

In this section, the effect of grain scattering noise on defect imaging is investigated. The total focusing method (TFM) [5] is selected as the imaging algorithm here as it is one of the most widely adopted advanced imaging approaches in NDT and provides high resolution throughout the component [22]. For a point (x, z), its imaging amplitude is given by TFM as [5]

$$I(x,z) = \left| \sum_{u,v} g(u,v,t = \frac{\sqrt{(u-x)^2 + z^2} + \sqrt{(v-x)^2 + z^2}}{c}) \right|, \tag{2}$$

where $g(u, v, t)$ denotes the signal measured by the transmitter-receiver pair where the locations of the transmitter and receiver elements are u and$v$, respectively (see Fig. 1(c)), and c is the ultrasonic velocity which can be calculated as described in Section 3.2. TFM is applied to the simulated array data of different target defects, and Fig. 3 shows the imaging results of cracks and holes of sizes 1mm and 3mm at 1-3MHz (frequency filters with 50% half bandwidth are applied to the array data in each figure). It is clearly seen from these figures that the TFM results progressively become dominated by grain noise as the frequency increases. When the defect size is 1mm, the crack and hole are seen to be indistinguishable from the image at all freqeuncies (in fact, they are undetectable when the frequency is 3 MHz). Although differences can be observed between the TFM images of the 3mm crack and 3mm hole shown in Figs. 3(c)-3(d) (*e.g.* the backwall indication at 1 MHz and defect indication at 2 MHz), accurate defect characterisation (*i.e.* sizing and determination of the defect type) from the image is difficult considering the small defect size and/or high noise levels.

Quantitatively, the images obtained at different frequencies can be compared by their SNR values, which are defined as

$$\mathrm{SNR} = 20 \times \log_{10} \frac{I_d}{n_{\mathrm{rms}}}. \tag{3}$$

In Eq. (3), I_d is the maximum image amplitude of the defect, and n_{rms} denotes the root-mean-square amplitude of the noise, which is calculated within a 10mm×10mm region on the left-hand-side of the defect and at a similar depth to the defect (*i.e.* the red box in Fig. 3(a)). Figures 4(a)-4(d) show the SNR results extracted from images such as those shown in Fig. 3 for 1mm cracks, 1mm holes, 3mm cracks, and 3mm holes, respectively. Within these results, each error bar shows the maximum and minimum image SNRs at a given frequency, and they are obtained from 50 random grain structures used to simulate the array data. The SNR values decrease as the frequency increases, and hence, the detection performance of ultrasonic inspection is shown to be governed by grain noise.

A detection threshold is needed to determine the existence of a defect. Figure 5 shows the distribution of the image amplitude within the noise region, obtained from 50 TFM images of 1mm cracks (the frequency is 3 MHz). As can be seen, noise amplitude in the image follows a Rayleigh distribution (red dashed line). Based on this observation, the detection threshold is set to be 12.4 dB (corresponding to the dashed lines in Figs. 4(a)-4(d)), and this gives a false call rate of 1/1000 for the considered image size in this report. It is noted that although the SNR threshold plays an important role in detection, its selection is “arbitrary” [23] in the sense that small defects may become detectable using low threshold values, but this could also result in high false alarm rates at the same time. By comparing the SNR results of cracks and holes of the same size, we find that although the detectability of a defect is primarily determiend by its size, holes are more

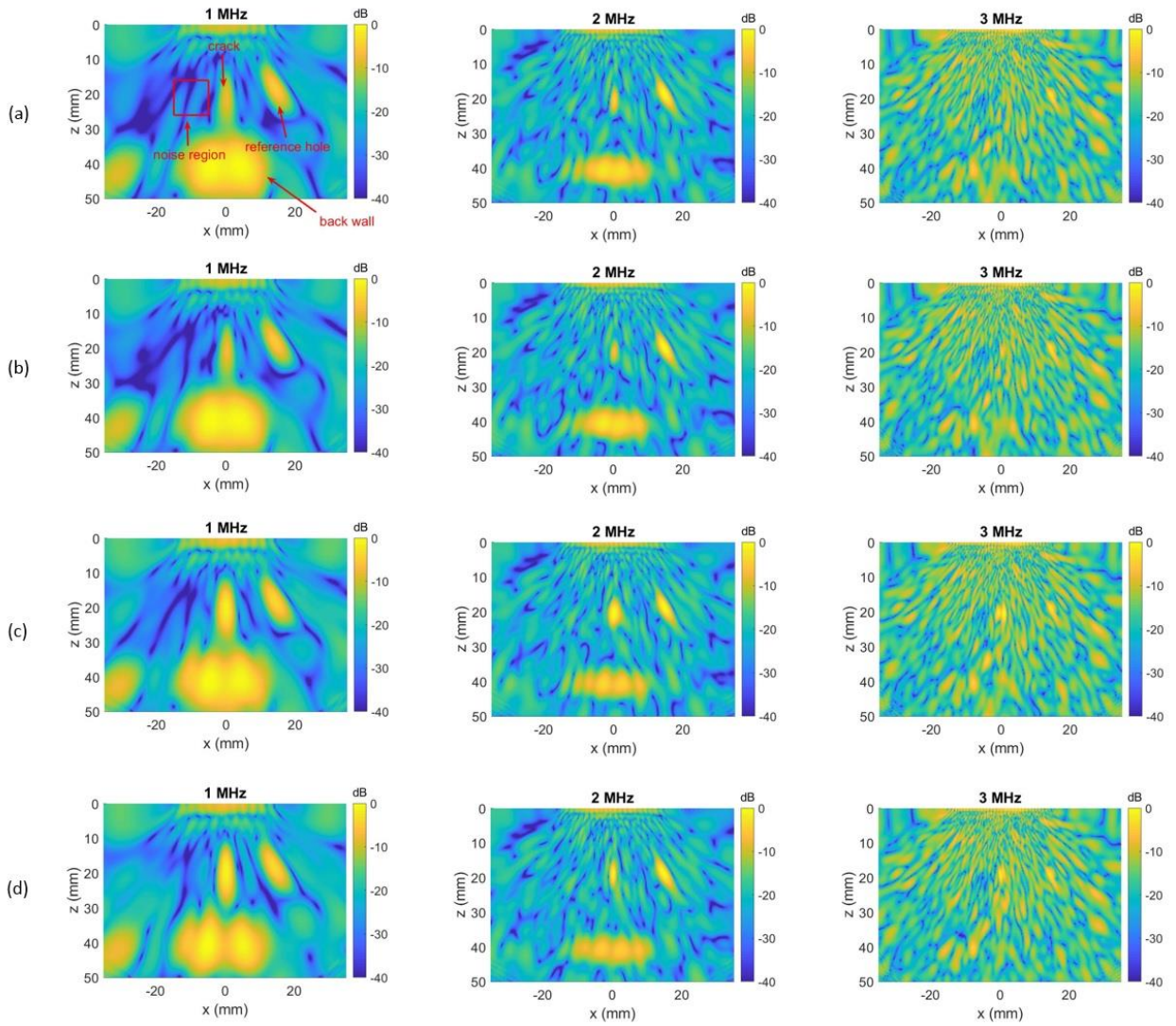

Figure 3: TFM results of the target defects and grains at 1-3 MHz, where (a) a 1mm crack, (b) a 1mm hole, (c) a 3mm crack, and (d) a 3mm hole.

Frequency (MHz)	Cracks			Holes		
	1mm	2mm	3mm	1mm	2mm	3mm
1	1	1	1	1	1	1
1.5	1	1	1	1	1	1
2	1	1	1	0.98	1	1
2.5	0.82	1	1	0.82	0.96	1
3	0.14	0.78	0.96	0.20	0.46	0.82

Table 1: Probability of detection (calculated from TFM images) of cracks and holes at different frequencies.

easily affected by grain noise compared to cracks of the same size. For example, the probability of detection is below 50% at 3 MHz for both 1mm cracks and 1mm holes (triangles in Fig. 4 represent the median SNR values) due to the small defect size. The minimum SNR of 3mm cracks is higher than that of 3mm holes at all frequencies and the difference in the minimun SNR value is above 1.5 dB except when the frequency is 1.5 MHz.

Table 1 summarises the probability of detection (calculated from 50 random grain structures as before) of the target defects. It can be seen that excellent probability of detection results are obtained at frequencies

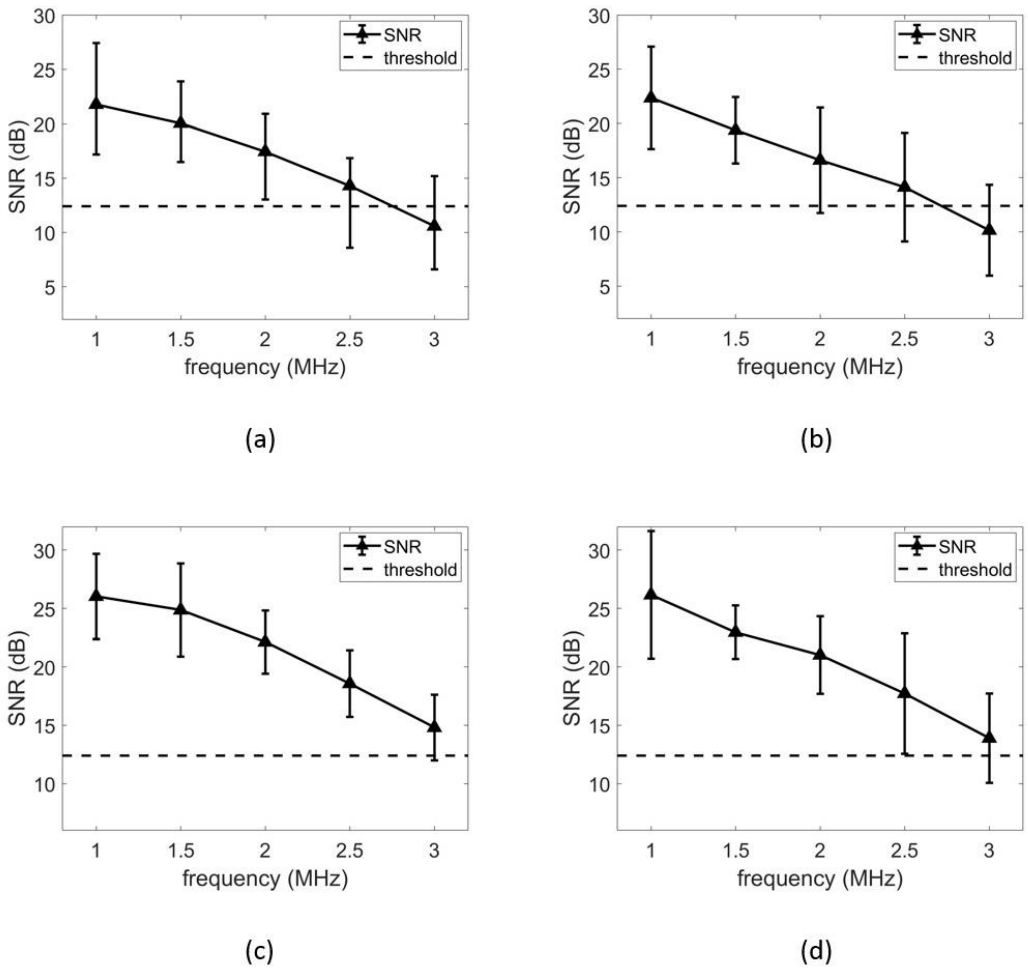

Figure 4: SNR results of (a) 1mm cracks, (b) 1mm holes, (c) 3mm cracks, and (d) 3mm holes. The error bars show the maximum and minimum image SNRs, and triangles represent the median SNRs (calculated from 50 random grain structures).

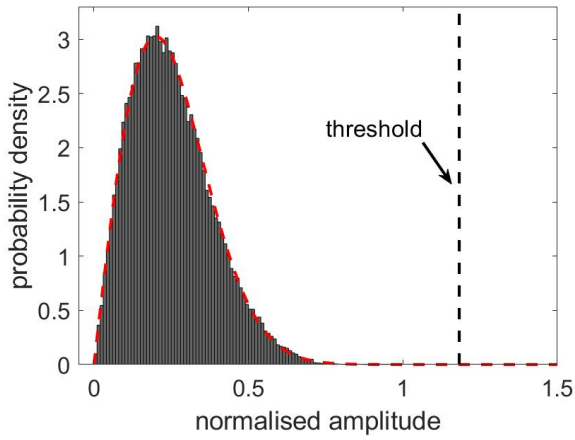

Figure 5: Histogram plot of the noise amplitude obtained from 50 TFM images of 1mm cracks when the frequency is 3 MHz. Red dashed line shows a Rayleigh distribution fitted to the noise data, and black dashed line corresponds to the SNR detection threshold of 12.4 dB.

1 MHz and 1.5 MHz for all defects. The probability of detection drops as the frequency increases, and cracks frequently achieved higher probability of detection compared to holes of the same size for a given frequency. This phenomenon can be explained by comparing the scattering matrices of different defects, as will be discussed in the next section. All cracks are assumed to be horizontal in the current work. The detectability of a crack is expected to drop if it has a large orientation angle (*i.e.* unfavourably oriented to the array), and

future work will aim to study the detection and characterisation problem of cracks with different orientation angles.

5 Detection and characterisation of defects using the scattering matrix

5.1 The scattering matrix

In this section, we consider using the scattering matrix for detection and characterisation of defects with the aim of improving the detection/characterisation accuracy. In a highly scattering medium, the scattering matrix can be defined as (assuming a 2D geometry as is shown in Fig. 1(c))

$$S(\theta_{\mathrm{in}}, \theta_{\mathrm{sc}}, \omega) = \frac{a_{\mathrm{sc}}(\omega)}{a_{\mathrm{in}}(\omega)} \sqrt{\frac{d_{\mathrm{sc}}}{\lambda}} \exp\left(-\frac{i\omega d_{\mathrm{sc}}}{c}\right) \exp[\alpha(\omega) d_{\mathrm{sc}}], \tag{4}$$

where θ_{in}, θ_{sc} are the incident and scattering angles, a_{in}, a_{sc} are the amplitude of the plane incident wave at the defect and scattered wave measured at a distance d_{sc} from the defect, respectively, c is the ultrasonic velocity, α is the attenuation coefficient, λ is the wavelength, and ω is the angular frequency. The scattering matrix encodes the information about a defect in the form of the scattering coefficients for all incident and scattering angles. Although the scattering matrix is defined for different mode combinations, only the longitudinal-incident-longitudinal-scattering waves are considered in this report. In addition, only the amplitude of the scattering matrix is extracted and used for characterisation because phase measurements are often associated with high uncertainty/large errors if the actual defect location is unknown [24].

The main advantage of using the scattering matrix for characterisation is that defects remain distinguishable and characterisable in terms of their scattering matrices even for small defect sizes. For example, Figs. 6(a)-6(b) show the noise-free scattering matrices of a 3mm crack and a 3mm hole at 2 MHz, where the incident and scattering angle ranges are the same as those measurable from the configuration shown in Fig. 1(b). The ultrasonic wavelength of the modelled material is 2.8mm when the frequency is 2 MHz, meaning that both defects are comparable to the wavelength in size. For the scattering matrix of the crack, high amplitude values are found when $\theta_{\mathrm{sc}} = -\theta_{\mathrm{in}}$ (corresponding to the specular reflection), and the amplitude of the pulse-echo component of the scattering matrix (*i.e.* $\theta_{\mathrm{sc}} = \theta_{\mathrm{in}}$) decreases quickly when the incident angle θ_{in} moves away from 0° (which corresponds to the normal-incidence-normal-scattering case). On the other hand, the most significant feature of the scattering matrix of a hole is that the scattering coefficient is a constant value in pulse-echo (in fact, the scattering coefficient is only dependent on the difference between the incident and scattering angles and is the same in every diagonal component of the scattering matrix). It is found that within the measurable angular range, the maximum amplitude of the scattering matrix of a crack is higher than that of a hole which has the same size as the crack. For the size range considered in this report, the difference in the scattering amplitude between cracks and holes is more significant for larger defects, and on average, the maximum scattering amplitude of a crack is 68% higher than that of a hole when the frequency is 2 MHz. The larger scattering amplitude of cracks can explain why the probability of detection is normally higher for cracks when compared to holes of the same size (see Table 1).

Figures 7(a)-7(b) show the scattering matrices of 3mm cracks and 3mm holes, respectively, at 2 MHz, obtained from 4 different random realisations of the grain structure. These scattering matrices are extracted from the simulated array data using the inverse imaging approach [25], and the 5mm hole (see Fig. 1(b)) is used as the reference defect for normalisation of the scattering amplitude. As shown in Figs. 7(a)-7(b), grain scattering introduces coherent noise to the measurement (*i.e.* it distorts the scattering matrix), and hence, degrades the characterisation performance. Although the scattering matrices of the cracks and holes still show different patterns, the effect of the grain scattering noise is also clearly observed in amplitude variations as well as a distortion of shape relative to the noise-free cases (Fig. 6). As a result, cracks can potentially be characterised as holes (or other volumetric defects such as ellipses) using classification

approaches if the noisy scattering matrices are compared to a pre-computed defect database including only the noise-free scattering matrices [13].

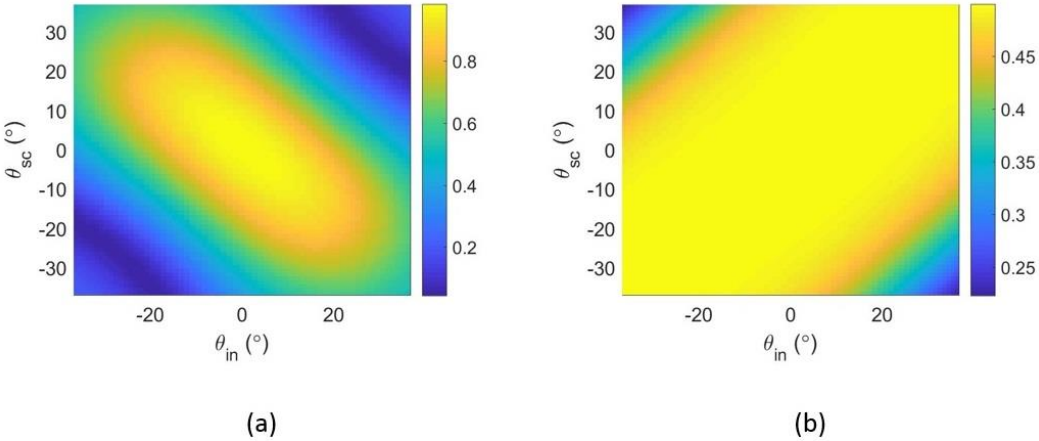

Figure 6: Noise-free scattering matrices of (a) a 3mm crack and (b) a 3mm hole, when the frequency is 2 MHz.

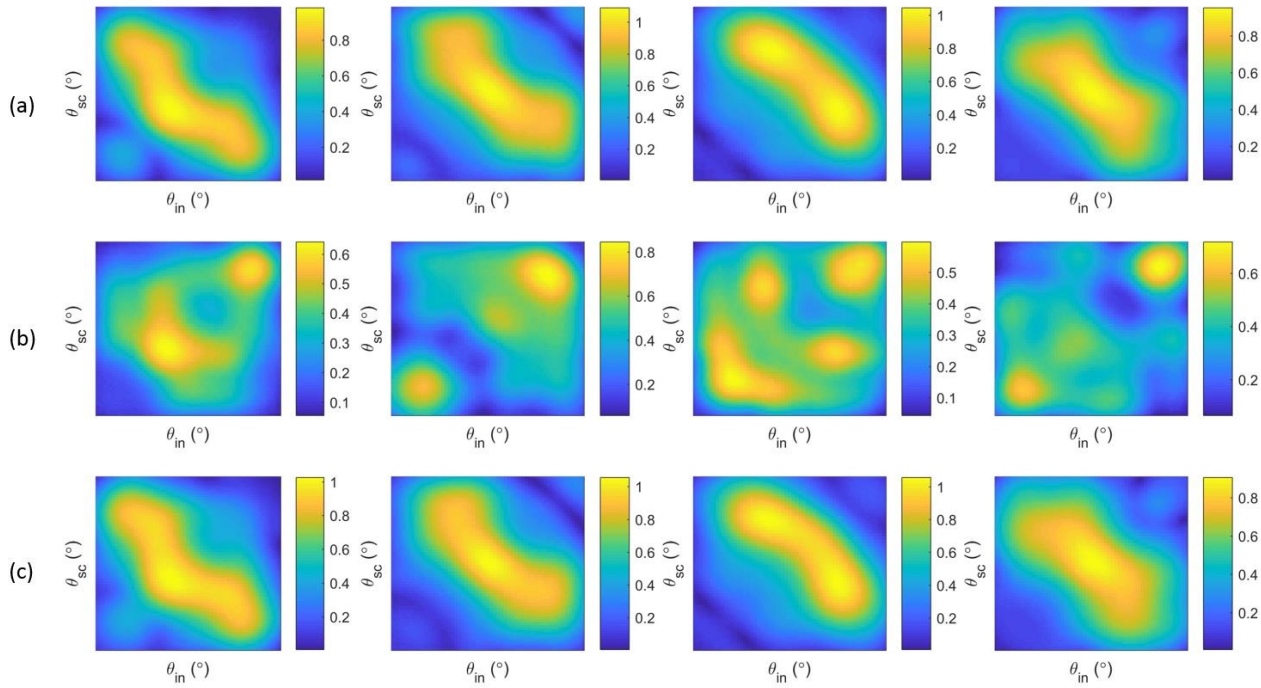

Figure 7: Scattering matrices of (a) 3mm cracks (element size in FE model: 80 µm), (b) 3mm holes (element size in FE model: 80 µm), and (c) 3mm cracks (element size in FE model: 40 µm), obtained from 4 random grain structures at 2 MHz. Incident and scattering angle ranges of the scattering matrices are the same as those shown in Fig. 6.

The default element size used in all FE simulations in this report is 80 μm as mentioned in Section 3. A smaller element size of 40 μm is used to simulate the array data of 3mm cracks for the same grain structures as the ones used in Fig. 7(a), and the extracted scattering matrices are shown in Fig. 7(c). The results in Fig. 7(c) are in good agreement with those in Fig. 7(a), confirming the accuracy of the FE model. More importantly, the difference between these two sets of results becomes even smaller when we compare the mean scattering matrices, and the relative difference is only 2.7%. This is important because grain noise modelling is based on calculating the statistics of the scattering matrices as will be discussed in the next section.

5.2 Defect characterisation approach

The key idea behind the defect characterisation approach adopted in this report can be described using Bayes theorem [8], [26]:

$$P(\boldsymbol{p}|\boldsymbol{S}_n) = \frac{P(\boldsymbol{S}_n|\boldsymbol{p})P(\boldsymbol{p})}{P(\boldsymbol{S}_n)}. \tag{5}$$

In Eq. (5), $P(\boldsymbol{p}|\boldsymbol{S}_n)$ denotes the conditional probability of the defect parameter $\boldsymbol{p}$ (*e.g.* representing size and/or type of a defect) given the measurement of the noisy scattering matrix $\boldsymbol{S}_n$ (*e.g.* the ones shown in Fig. 7), and is the desired output of the defect characterisation process [8]. If we assume that the occurrence of different defects and scattering matrices are equally probable (*i.e.* $\boldsymbol{p}$ and $\boldsymbol{S}_n$ are uniformly distributed), Eq. (5) reduces to

$$P(\boldsymbol{p}|\boldsymbol{S}_n) = CP(\boldsymbol{S}_n|\boldsymbol{p}), \tag{6}$$

where C is a normalisation constant that can be calculated from $C = (\int P(\boldsymbol{S}_n|\boldsymbol{p})dp)^{-1}$. It can be seen from Eq. (6) that the conditional probability of the defect parameter $\boldsymbol{p}$ given the measurement of the noisy scattering matrix $\boldsymbol{S}_n$ is proportional to the probability of measuring $\boldsymbol{S}_n$ from a defect which can be described by parameter $\boldsymbol{p}$ with the presence of grain scattering noise. Note that prior knowledge about the defect parameter $\boldsymbol{p}$ can be readily incorporated into the Bayesian framework described above, in which case different normalisation constants need to be used for different defects [8]. In this report, C is assumed to be a constant for simplicity. Because any real experimental measurement can be written as $\boldsymbol{S}_n = \boldsymbol{S}_0 + \boldsymbol{n}$ where $\boldsymbol{S}_0$ is the noise-free scattering matrix and $\boldsymbol{n}$ represents measurement noise, the conditional probability $P(\boldsymbol{S}_n|\boldsymbol{p})$ can also be expressed in the form $P(\boldsymbol{n}|\boldsymbol{p})$. This indicates that an understanding of the noise distribution $P(\boldsymbol{n}|\boldsymbol{p})$ (referred to as the noise model in this report) is crucial in determining the characterisation uncertainty using Eq. (6). We can calculate the statistics of the noise model based on multiple random realisations of the grain structure, and term this method the "noise modelling approach". It is worth emphasizing that the selection of the statistical model of the grain noise distribution is dependent on the available training (*i.e.* simulation or experimental) data only, and is not based on any prior assumtions.

The measurement noise $\boldsymbol{n}$ ($\in \mathbb{R}^{N\times N}$ where N is the number of incident/scattering angles) normally has thousands of noise coefficients, each corresponding to a specific transmitter-receiver pair of the array. To avoid building a statistical distribution which has excessively large number of variables, $\boldsymbol{n}$ is transformed into a lower dimensional space by the use of principal component analysis (PCA) [27]. PCA is able to identify a small number of "directions" (termed the principal components or PCs) which are responsible for most of the variation in a data set. For statistical confidence, a large number of noise data are required for the PCA process. In this report, we used a total of 350 noise realisations for a given frequency (obtained for 6 target defect cases, *i.e.* cracks and holes of sizes 1-3mm, as well as a non-defect case, each with 50 random grain structres) when performing PCA. The variation explained by the first 30 principal component directions (for the frequency of 2 MHz) is shown in Fig. 8, which indicates that the majority of information in the measurement noise due to grain scattering can indeed be encoded by a small number of the principal components. These principal components form the coordinate axes of a new space in which the noise models are constructed, and this new corrdinate system is termed the noise PC-space [8] hereafter. Following this, the noise model used for characterisation can now be expressed as $P(\boldsymbol{n}^{\mathrm{pc}}|\boldsymbol{p})$ where $\boldsymbol{n}^{\mathrm{pc}}$ denotes noise $\boldsymbol{n}$ in the noise PC-space.

For measurement noise caused by grain scattering, a critical observation is that the statistical distribution of the noise $\boldsymbol{n}^{\mathrm{pc}}$ is related to the defect parameter $\boldsymbol{p}$. This can be seen from Figs. 9(a)-9(b) which show the distribution of grain noise for cracks and holes, respectively, in the first PC-direction at the frequency of 3 MHz. Importantly, we find that the probability density function of the grain noise distribution of non-defect

cases (red lines in Fig. 9) is different from those of the defects, which can be used to distinguish between defect- and noise- scattering matrices. This is shown to improve the detection performance compared to image-based methods, as will be discussed in the next section.

Because the probability density functions shown in Fig. 9 have shapes similar to those of Gaussian distributions, it is reasonable to use a multivariate Gaussian distribution [8] to model the noise distribution in the noise PC-space. Hence, a noise model can be expressed as

$$P(\boldsymbol{n}^{\mathrm{pc}}|\boldsymbol{p}) = \frac{1}{(2\pi)^{N_p/2}|\boldsymbol{\Sigma}|^{1/2}} \exp\left[-\frac{1}{2}(\boldsymbol{n}^{\mathrm{pc}} - \boldsymbol{\mu})^{\mathrm{T}}\boldsymbol{\Sigma}^{-1}(\boldsymbol{n}^{\mathrm{pc}} - \boldsymbol{\mu})\right], \tag{7}$$

where N_p is the number of noise PCs (the first 10 noise PCs are used for characterisation in this report as the variance is shown to converge when the PC index is 10 in Fig. 8, and adding more PCs can potentially allow more noise within the array data to be used for characterisation). $\boldsymbol{\mu}$ and $\boldsymbol{\Sigma}$ denote the mean and covariance matrix, respectively, and can be estimated from the available training data by

$$\boldsymbol{\mu} = \sum_{i=1}^{M} \boldsymbol{n}_i^{\mathrm{pc}}/M, \tag{8}$$

$$\boldsymbol{\Sigma} = \sum_{i=1}^{M} \left(\boldsymbol{n}_i^{\mathrm{pc}} - \boldsymbol{\mu}\right)\left(\boldsymbol{n}_i^{\mathrm{pc}} - \boldsymbol{\mu}\right)^{\mathrm{T}}/(M-1). \tag{9}$$

In Eqs. (8)-(9), M = 50 is the number of the noise scattering matrices modelled in forward simulation for a given target defect, and $\boldsymbol{n}_i^{\mathrm{pc}}$ denotes the i-th training data. In summary, the defect characterisation approach based on the scattering matrix can be described algorithmically as follows:

- Step 1: Apply TFM or other imaging algorithms to array data and identify (from the image) regions of interest which could potentially contain defects.
- Step 2 : Extract the scattering matrix $\boldsymbol{S}_n$ from a region of interest identified at Step 1, calculate the noise $\boldsymbol{n}$ and convert it into the noise PC-space to obtain $\boldsymbol{n}^{\mathrm{pc}}$. Given a defect parameter $\boldsymbol{p}$, the measurement noise $\boldsymbol{n}$ is the difference between $\boldsymbol{S}_n$ and noise-free scattering matrix $\boldsymbol{S}_p$ of the defect.

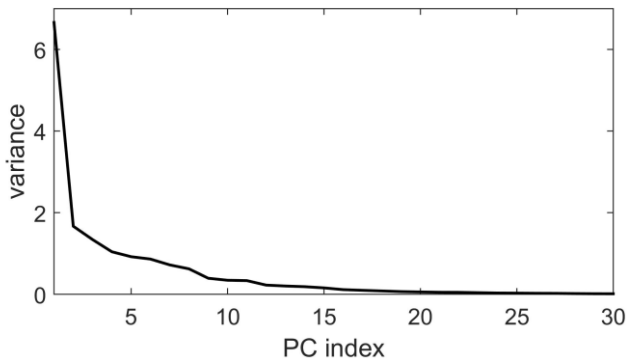

Figure 8: Variance explained by the first 30 principal component directions of the noise PC-space.

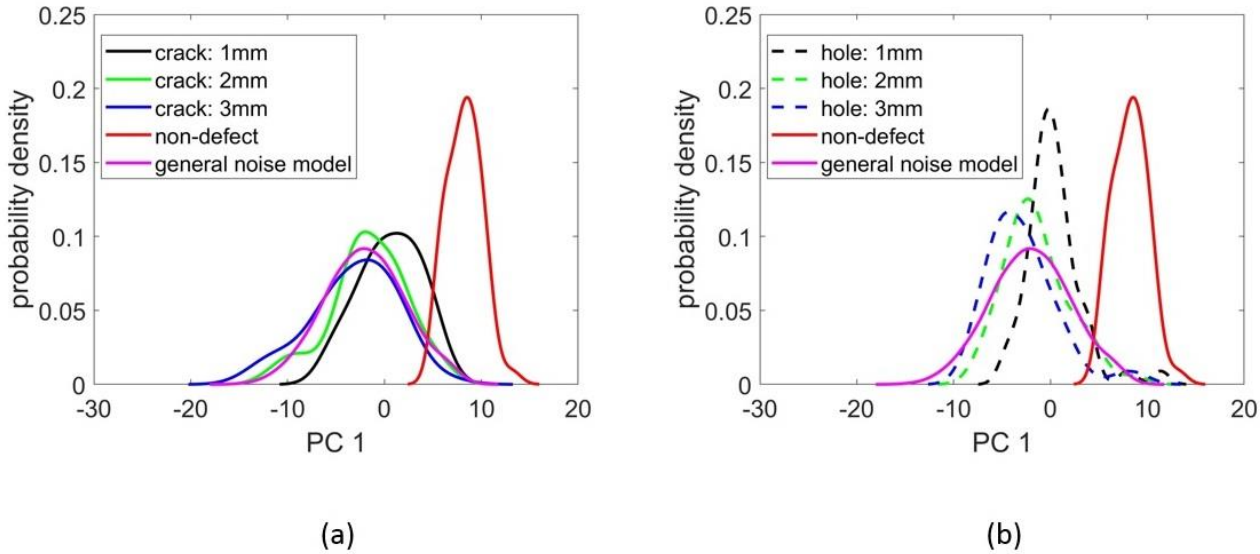

Figure 9: Grain noise distribution of different defects and the general noise model [8].

- Step 3 : Calculate the conditional probability $P(\boldsymbol{n}^{\mathrm{pc}}|\boldsymbol{p})$ for each target defect.
- Step 4 : The defect characterisation result can be obtained as $P(\boldsymbol{p}|\boldsymbol{n}^{\mathrm{pc}}) = CP(\boldsymbol{n}^{\mathrm{pc}}|\boldsymbol{p})$, where $C = (\int P(\boldsymbol{n}^{\mathrm{pc}}|\boldsymbol{p})dp)^{-1}$.

5.3 Results

In this section, the performance of the defect characterisation approach is studied by characterising test data which were not used for noise modelling. For each target defect, scattering matrices are extracted from simulated array data based on 10 new grain structures, and the average characterisation results (obtained at 2 MHz) are shown in Figs. 10(a)-10(f). In each figure, the green bar (corresponding to the size 0) gives the probability that the target defect is undetected (*i.e.* identified as grain noise). In addition, the red and blue bars show the probabilities of the defect being cracks and holes of sizes 1-3mm, and the bar corresponding to the actual modelled defect is indicated with an arrow. From the results of the cracks (Figs. 10(a)-10(c)), it is seen that cracks can be characterised accurately with higher confidence as the crack size increases. For the results of the holes (Figs. 10(d)-10(f)), however, uncertainty remains high for all defect sizes considered. Also, it is found that the false negative rate of 1mm holes (corresponding to the height of the green bar in Fig. 10(d)) is higher than that of 1mm cracks. This is believed to be related with the lower amplitude of the scattering matrices of the holes, when compared to cracks of the same size.

One of the main improvements achieved in the current work compared to previous works [8], [24] is that actual grain scattering noise is modelled and used for characterisation instead of making prior assumptions about the noise distribution. On the contrary, under the general coherent noise assumption, noise was previously modelled to have the same distribution as that of two-dimensional Gaussian random rough surfaces [28]. The same paramters for describing a rough surface in 2D were used for describing general coherent noise (see [8] for more details), and the mean value of the noise was assumed to be 0. Although the covariance matrix $\boldsymbol{\Sigma}$ (see Eq.(9)) of the Gaussian distribution can be made close to the true value (*e.g.* by optimising parameters of the general coherent noise model), the noise distribution obtained with this zero-mean assumption could potentially lead to poor characterisation results. Figure 11(a) shows the characterisation result of the non-defect cases which is obtained from 10 new grain structures as before. The actual noise models (*i.e.* mean and covariance matrix are calculated from the training data) are used in Fig. 11(a), and the considered frequency is 3 MHz as the effect of grain scattering noise is most significant

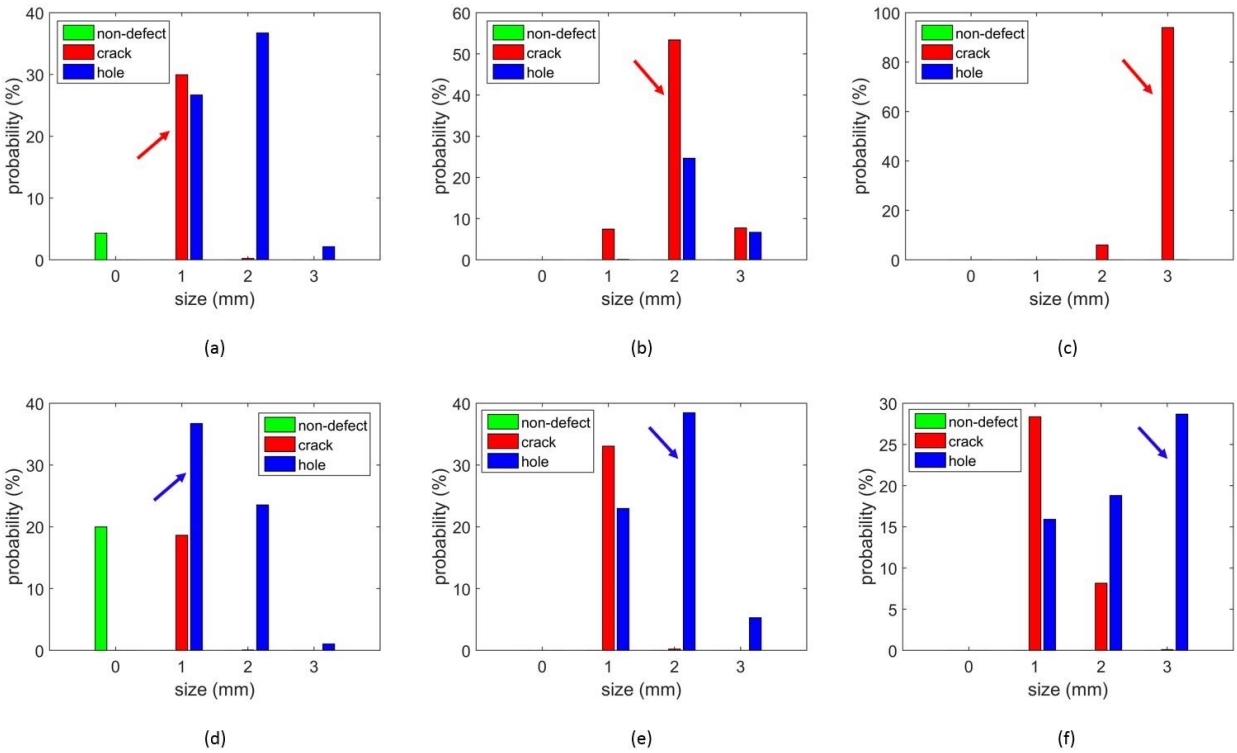

Figure 10: Average characterisation results of different defects when the frequency is 2 MHz, where (a) 1mm cracks, (b) 2mm cracks, (c) 3mm cracks, (d) 1mm holes, (e) 2mm holes, and (f) 3mm holes. In each figure, the bar corresponding to the actual modelled defect is indicated with an arrow.

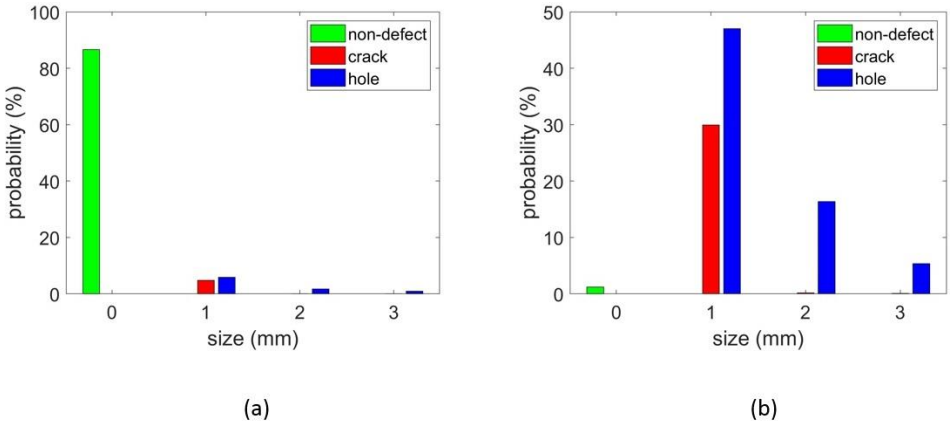

Figure 11: Characterisation results of non-defect cases when the frequency is 3 MHz, where (a) the actual noise models and (b) the general coherent noise model [8], are used for characterisation.

at this high frequency. We can see that false alarms do appear due to the high noise level but the probability of the correct category (*i.e.* 'non-defect') is still dominant (86.6%). Figure 11(b) shows the result obtained with the use of a general coherent noise model [8]. It can be seen that the general noise model has yielded poor characterisation result with the false alarm rate of 98.8%, although the parameters of the noise model are carefully selected using the maximum-likelihood estimation method [24]. This is not surprising because the probability density function of the general noise model is indeed more similar to the actual noise distribution of the defects than that of non-defect cases as can be seen from Fig. 9.

It is important to study the effect of the inspection frequency on detection/characterisation performance of the proposed approach. Here, we use probability of detection, classification accuracy, and sizing error to compare the results obtained at different frequencies. Probability of detection gives the probability that a

defect can be distinguished from noise, and is related to the detectability of a defect. Classification accuracy is defined as the probability that the defect type is correctly identified (*e.g.* sum of the probability of the red bars in Figs. 10(a)-10(c) or sum of the blue bars in Figs. 10(d)-10(f)), and the sizing error is given as the difference between the mean sizing result and the actual defect size. These results are summarised in Tables 2-4 for the target defects at frequencies 1-3 MHz. From the probability of detection result given in Table 2, we find that all the defects can be detected with high confidence at 1 MHz and 1.5 MHz. For cracks and holes of sizes 1mm and 2mm, a drop in the probability of detection is observed as the frequency increases, and importantly, the detection performance is improved compared to the image-based inspection at 3 MHz (see Table 1). The classification accuracy of 1mm cracks is shown to be poor at all frequencies. 2mm cracks can be classified accurately at frequencies between 1.5 MHz and 3 MHz, and their sizing error is relatively small at all frequencies. At 1.5-2.5 MHz, 3mm cracks are shown to achieve excellent characterisation with high classification accuracy and small sizing errors, but their sizing errors at 1 MHz and 3 MHz are large. The classification accuracy of the holes is satisfactory for most cases, but holes also tend to have larger sizing errors than cracks.

Frequency (MHz)	Cracks			Holes		
	1mm	2mm	3mm	1mm	2mm	3mm
1	1	1	1	1	1	1
1.5	1	1	1	1	1	1
2	0.96	1	1	0.80	1	1
2.5	0.96	1	1	0.81	1	1
3	0.46	0.98	1	0.97	0.57	1

Table 2: Probability of detection (calculated using the scattering matrix) of cracks and holes at different frequencies.

Frequency (MHz)	Cracks			Holes		
	1mm	2mm	3mm	1mm	2mm	3mm
1	0.34	0.56	0.88	0.92	0.98	1
1.5	0.47	0.88	1	0.56	0.73	0.99
2	0.30	0.69	1	0.61	0.67	0.63
2.5	0.41	0.71	1	0.46	0.77	0.58
3	0.18	0.73	0.84	0.72	0.44	0.68

Table 3: Classification accuracy (calculated using the scattering matrix) of cracks and holes at different frequencies.

Frequency (MHz)	Cracks			Holes		
	1mm	2mm	3mm	1mm	2mm	3mm
1	0.17	0.10	0.36	0.33	0.13	0.02
1.5	0.04	0.19	4.13×10^{-3}	0.32	0.11	0.66
2	0.37	0.07	0.06	0.06	0.51	1.16
2.5	0.27	0.11	0.03	0.05	0.63	1.36
3	0.38	0.22	0.58	0.33	1.26	1.00

Table 4: Mean sizing error (mm, calculated using the scattering matrix) of cracks and holes at different frequencies.

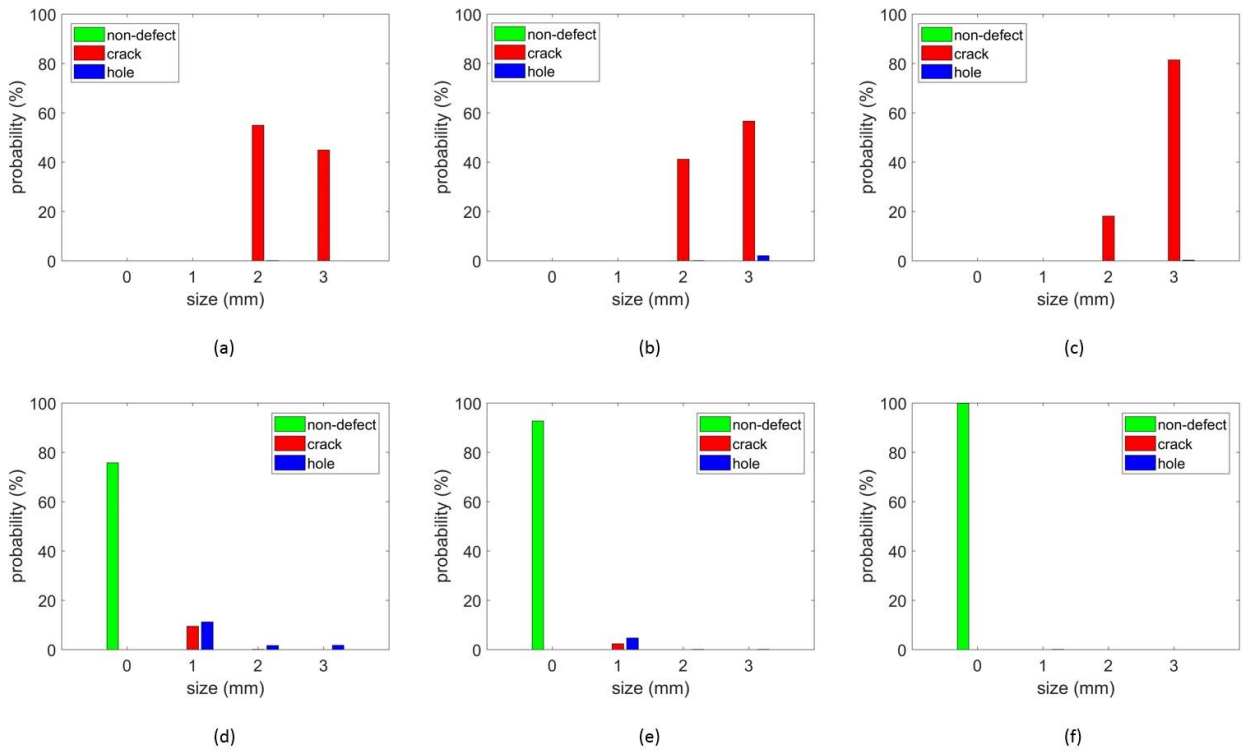

Figure 12: Characterisation results obtained with different number of array elements: (a) 3mm cracks with 16 elements, (b) 3mm cracks with 32 elements, (c) 3mm cracks with 48 elements, (d) non-defect cases with 16 elements, (e) non-defect cases with 32 elements, and (f) non-defect cases with 48 elements.

Array aperture size is another important parameter related to the inspection accuracy of an array. In order to study its effect on detection and characterisation of defects, characterisation results obtained with arrays having different number of elements are compared in Fig. 12 (the same element pitch of 0.5mm is used in all cases and the range of accessible incident/scattering angles increases by using more array elements). Figures 12(a)-12(c) show the characterisation results of 3mm cracks at 2 MHz when the number of array element is 16, 32, and 48, respectively. Compared to the characterisation result shown in Fig. 10(c) which is obtained with a 64 element array, the sizing uncertainty can be seen to increase as the number of array elements decreases and the defect size is underestimated with increasing probability. The reduction in the number of array elements also causes difficulty in distinguishing between defects and grain indications in an image. Figures 12(d)-12(f) show the charactersation results of the non-defect cases obtained with 16, 32, and 48 array elements, and false alarms are shown to appear in Figs. 12(d)-12(e) even at the relatively low frequency of 2 MHz.

6 Conclusions

Grain scattering noise is modelled and used for evaluating the characterisation uncertainty in this report. Firstly, a grain structure is simulated as a Voronoi diagram that can be obtained from randomly shifted nodes (corresponding to the vertexes of a grain). Secondly, an FE model is prepared by introducing a target defect into the simulated grain structure, and the array data is computed by running FE simulations. Thirdly, the scattering matrix of the defect is extracted from the simulated array data, and is used as the basis for the proposed characterisation approach.

By comparing to the use of general noise models, the proposed noise modelling approach shows that forward modelling based on *a priori* knowledge about the grain size distribution within a material and anisotropic material properties can provide important information that is useful for accurate detection and characterisation of defects. Using the proposed approach, characterisation accuracy calculated from the test dataset is shown to be different for different defects. For example, 3mm cracks can be detected, classified and sized with excellent accuracy when the frequency is between 1.5 MHz and 2.5 MHz. However, the classification accuracy of 1mm cracks is consistently poor at all frequencies considered, while their sizing results are still acceptable at 1-1.5 MHz.

In practice, the proposed defect characterisation approach requires knowledge about the grain size distribution and anisotropic material properties of the test sample, which can be used in FE simulations to obtain multiple realisations of the noise scattering matrix. Alternatively, noise can be measured experimentally from different regions of a sample or samples which are known to have similar grain structures. Future work will aim to study the performance of the noise modelling approach by characterising real defects that are found in industrially relevant samples.

7 Bibliography

[1] J. D. Achenbach, “Quantitative nondestructive evaluation,” *Int. J. Solids Struct.*, vol. 37, no. 1-2, pp. 13–27, 2000.

[2] T. Kundu, *Ultrasonic nondestructive evaluation: Engineering and biological material characterization*. CRC Press, 2004.

[3] S. J. Song, H. J. Shin, and Y. H. Jang, “Development of an ultrasonic phased array system for nondestructive tests of nuclear power plant components,” *Nucl. Eng. Design*, vol. 214, no. 1-2, pp. 151–161, 2002.

[4] B. W. Drinkwater and P. D. Wilcox, “Ultrasonic arrays for non-destructive evaluation: A review,” *NDT E Int.*, vol. 39, no. 7, pp. 525–541, 2006.

[5] C. Holmes, B. W. Drinkwater, and P. D. Wilcox, “Post-processing of the full matrix of ultrasonic transmit-receive array data for nondestructive evaluation,” *NDT E Int.*, vol. 38, no. 8, pp. 701–711, 2005.

[6] N. Pörtzgen, D. Gisolf, and G. Blacquiere, “Inverse wave field extrapolation: A different NDI approach to imaging defects,” *IEEE Trans. Ultrason. Ferroelectr. Freq. Control*, vol. 54, no. 1, pp. 118–127, 2007.

[7] A. J. Hunter, B. W. Drinkwater, and P. D. Wilcox, “The wavenumber algorithm for full-matrix imaging using an ultrasonic array,” *IEEE Trans. Ultrason. Ferroelectr. Freq. Control*, vol. 55, no. 11, pp. 2450–2462, 2008.

[8] A. Velichko, L. Bai, and B. W. Drinkwater, “Ultrasonic defect characterisation using parametric-manifold mapping,” *Proc. R. Soc. A*, vol. 473, no. 2202, p. 20170056, 2017.

[9] L. J. Cunningham, A. J. Mulholland, K. M. Tant, A. Gachagan, G. Harvey, and C. Bird, “The detection of flaws in austenitic welds using the decomposition of the time-reversal operator,” *Proc. R. Soc. A*, vol. 472, no. 2188, p. 20150500, 2016.

[10] A. Van Pamel, P. B. Nagy, and M. J. Lowe, “On the dimensionality of elastic wave scattering within heterogeneous media,” *J. Acoust. Soc. Am.*, vol. 140, no. 6, pp. 4360–4366, 2016.

[11] H. A. Bloxham, A. Velichko, and P. D. Wilcox, “Establishing the limits of validity of the superposition of experimental and analytical ultrasonic responses for simulating imaging data,” *IEEE Trans. Ultrason. Ferroelectr. Freq. Control*, vol. 66, no. 1, pp. 101–108, 2019.

[12] F. J. Margetan, R. B. Thompson, and I. Yalda-Mooshabad, “Backscattered microstructural noise in ultrasonic toneburst inspections,” *J. Nondestruct. Eval.*, vol. 13, no. 3, pp. 111–136, 1994.

[13] L. Bai, A. Velichko, and B. W. Drinkwater, “Characterization of defects using ultrasonic arrays: A dynamic classifier approach,” *IEEE Trans. Ultrason. Ferroelectr. Freq. Control*, vol. 62, no. 12, pp. 2146–2160, 2015.

[14] F. Xie, L. Moreau, Y. Zhang, and E. Larose, “A Bayesian approach for high resolution imaging of small changes in multiple scattering media,” *Ultrasonics*, vol. 64, pp. 106–114, Jan. 2016.

[15] A. Van Pamel, G. Sha, S. I. Rokhlin, and M. J. Lowe, “Finite-element modelling of elastic wave propagation and scattering within heterogeneous media,” *Proc. R. Soc. A*, vol. 473, no. 2197, p. 20160738, 2017.

[16] F. Aurenhammer, “Voronoi diagrams-A survey of a fundamental geometric data structure,” *ACM Comput. Surveys*, vol. 23, no. 3, pp. 345–405, 1991.

[17] S. Ahmed and R. B. Thompson, “Propagation of elastic waves in equiaxed stainless-steel polycrystals with aligned [001] axes,” *J. Acoust. Soc. Am.*, vol. 99, no. 4, pp. 2086–2096, 1996.

[18] D. S. Kupperman and K. J. Reimann, “Effect of shear-wave polarization on defect detection in stainless steel weld metal,” *Ultrasonics*, vol. 16, no. 1, pp. 21–27, 1978.

[19] P. Huthwaite, “Accelerated finite element elastodynamic simulations using the GPU,” *J. Comput. Phys.*, vol. 257, pp. 687–707, Jan. 2014.

[20] M. Sutcliffe, M. Weston, B. Dutton, P. Charlton, and K. Donne, “Real-time full matrix capture for ultrasonic non-destructive testing with acceleration of post-processing through graphic hardware,” *NDT E Int.*, vol. 51, pp. 16–23, Oct. 2012.

[21] H. A. Bloxham, A. Velichko, and P. D. Wilcox, “Combining simulated and experimental data to simulate ultrasonic array data from defects in materials with high structural noise,” *IEEE Trans. Ultrason. Ferroelectr. Freq. Control*, vol. 63, no. 12, pp. 2198–2206, 2016.

[22] M. Sutcliffe, P. Charlton, and M. Weston, “Multiple virtual source aperture imaging for non-destructive testing,” *Insight*, vol. 56, no. 2, pp. 75–81, 2014.

[23] N. Brierley, T. Tippetts, and P. Cawley, “Data fusion for automated non-destructive inspection,” *Proc. R. Soc. A*, vol. 470, no. 2167, p. 20140167, 2014.

[24] L. Bai, A. Velichko, and B. W. Drinkwater, “Ultrasonic defect characterisation - Use of amplitude, phase, and frequency information,” *J. Acoust. Soc. Am.*, vol. 143, no. 1, pp. 349–360, 2018.

[25] A. Velichko and P. D. Wilcox, “Reversible back-propagation imaging algorithm for postprocessing of ultrasonic array data,” *IEEE Trans. Ultrason. Ferroelectr. Freq. Control*, vol. 56, no. 11, pp. 2492–2503, 2009.

[26] T. Hastie, R. Tibshirani, and J. Friedman, *The elements of statistical learning,* 2nd ed. Springer-Verlag, 2009.

[27] I. T. Jolliffe, *Principal component analysis,* 2nd ed. Springer-Verlag, 2002.

[28] F. Shi, W. Choi, M. J. Lowe, E. A. Skelton, and R. V. Craster, “The validity of Kirchhoff theory for scattering of elastic waves from rough surfaces,” *Proc. R. Soc. A*, vol. 471, no. 2178, p. 20140977, 2015.

